CONDENSED MATTER PHYSICS

An all-epitaxial nitride heterostructure with concurrent quantum Hall effect and superconductivity

Phillip Dang[1]*, Guru Khalsa[2]*, Celesta S. Chang[1,3], D. Scott Katzer[4], Neeraj Nepal[4], Brian P. Downey[4], Virginia D. Wheeler[4], Alexey Suslov[5], Andy Xie[6], Edward Beam[6], Yu Cao[6], Cathy Lee[6], David A. Muller[1,7], Huili Grace Xing[2,7,8], David J. Meyer[4], Debdeep Jena[2,7,8]*

Creating seamless heterostructures that exhibit the quantum Hall effect and superconductivity is highly desirable for future electronics based on topological quantum computing. However, the two topologically robust electronic phases are typically incompatible owing to conflicting magnetic field requirements. Combined advances in the epitaxial growth of a nitride superconductor with a high critical temperature and a subsequent nitride semiconductor heterostructure of metal polarity enable the observation of clean integer quantum Hall effect in the polarization-induced two-dimensional (2D) electron gas of the high-electron mobility transistor. Through individual magneto-transport measurements of the spatially separated GaN 2D electron gas and superconducting NbN layers, we find a small window of magnetic fields and temperatures in which the epitaxial layers retain their respective quantum Hall and superconducting properties. Its analysis indicates that in epitaxial nitride superconductor/semiconductor heterostructures, this window can be significantly expanded, creating an industrially viable platform for robust quantum devices that exploit topologically protected transport.

INTRODUCTION

Integer quantum Hall effect (IQHE) edge states in a semiconductor two-dimensional electron gas (2DEG) remain the paragon of topologically protected conductance quantization in electron transport (*1*, *2*). Topological protection of the phase of Cooper pairs on the other hand manifests as flux quantization in superconducting weak links (*3*). Because of the high precision, of more than a part in a billion, conductance quantization in the IQHE state in semiconductors forms the modern resistance standard, while flux quantization in superconductors is the modern voltage standard (*4*). To date, the IQHE has not been observed in a semiconductor 2DEG that is epitaxially grown on a superconductor. Typically, a robust IQHE state requires a magnetic field, which generally destroys superconductivity by the Meissner effect, preventing the two from coexisting. In this work, we report the realization of an epitaxial heterostructure in which the 2DEG of the high electron mobility transistor (HEMT) exhibits the IQHE in a regime where an underlying, spatially separated superconductor retains its superconducting properties.

By exploiting the similarity of crystal structures and chemical properties of the GaN family of semiconductors with the nitride superconductor NbN, the realization of their epitaxial heterostructure was recently reported (*5*). In that work, weak Shubnikov–de Haas oscillations were observed in a 2DEG in a nitride heterostructure fabricated on NbN, both of which were grown epitaxially. The magnetotransport properties of the 2DEG in that study were far from the IQHE state, and the magnetic fields at which the Shubnikov–de Haas oscillations were observed were much larger than the critical Meissner field H_c of the epitaxial superconducting NbN. In this work, a modified epitaxial growth process is found to (i) lead to a much sharper Tc and a higher Hc of the superconducting NbN and (ii) flip the crystal lattice polarity in the nitride heterostructure, resulting in a strong and clean IQHE in the 2DEG of the HEMT. These improvements enable the two phenomena, IQHE and superconductivity, to simultaneously occur in a single nanoscale device over a narrow range of temperatures and magnetic fields. This observation, and the transport properties of nitride 2DEGs, indicates that the range of temperatures and magnetic fields in which superconductivity of NbN and the IQHE in the GaN 2DEG can simultaneously occur can be significantly increased in this family of epitaxial semiconductor/superconductor heterostructures.

RESULTS

2DEGs in AlGaAs/GaAs heterostructures are formed by intentional modulation doping of donor dopants in the wider-bandgap semiconductor barrier. In AlGaN/GaN heterostructures, the 2DEG is of a fundamentally different origin: It is formed because of the Berry phase–driven electronic polarization discontinuity across the heterojunction (*6*). Therefore, the polarity (metal versus N polar) of the crystal uniquely determines the heterojunction at which the 2DEG is formed. Figure 1A shows a scanning transmission electron microscopy (STEM) image of the entire heterostructure used in this work. Figure 1 (B and C) zooms in on the nitride layers that contain the 2DEG. While the crystal lattice in the all-MBE heterostructure studied in (*5*) was N-polar in which the 2DEG was located above the epitaxial barrier layer, the metalorganic chemical vapor deposition (MOCVD) grown sample reported here is metal-polar, as shown in Fig. 1D. In Fig. 1D, the metal (larger circle) forms a chemical bond to the nitrogen atom (smaller circle) vertically above it: a fingerprint of metal polarity. This positions the 2DEG below the epitaxial AlGaN barrier layer, as confirmed by the measured gate capacitance. Because the superconducting NbN layer is cubic and nonpolar (Fig. 1E), the polarity in the structure begins with the AlN nucleation layer grown on NbN. The metal polarity is seen to be fixed from this nucleation

[1]School of Applied and Engineering Physics, Cornell University, Ithaca, NY 14853, USA. [2]Department of Materials Science and Engineering, Cornell University, Ithaca, NY 14853, USA. [3]Department of Physics, Cornell University, Ithaca, NY 14853, USA. [4]United States Naval Research Laboratory, Washington, DC 20375, USA. [5]National High Magnetic Field Laboratory, Tallahassee, FL 32310, USA. [6]Qorvo, Richardson, TX 75080, USA. [7]Kavli Institute at Cornell for Nanoscale Science, Cornell University, Ithaca, NY 14853, USA. [8]School of Electrical and Computer Engineering, Cornell University, Ithaca, NY 14853, USA.
*Corresponding author. Email: pd382@cornell.edu (P.D.); gsk63@cornell.edu (G.K.); djena@cornell.edu (D.J.)

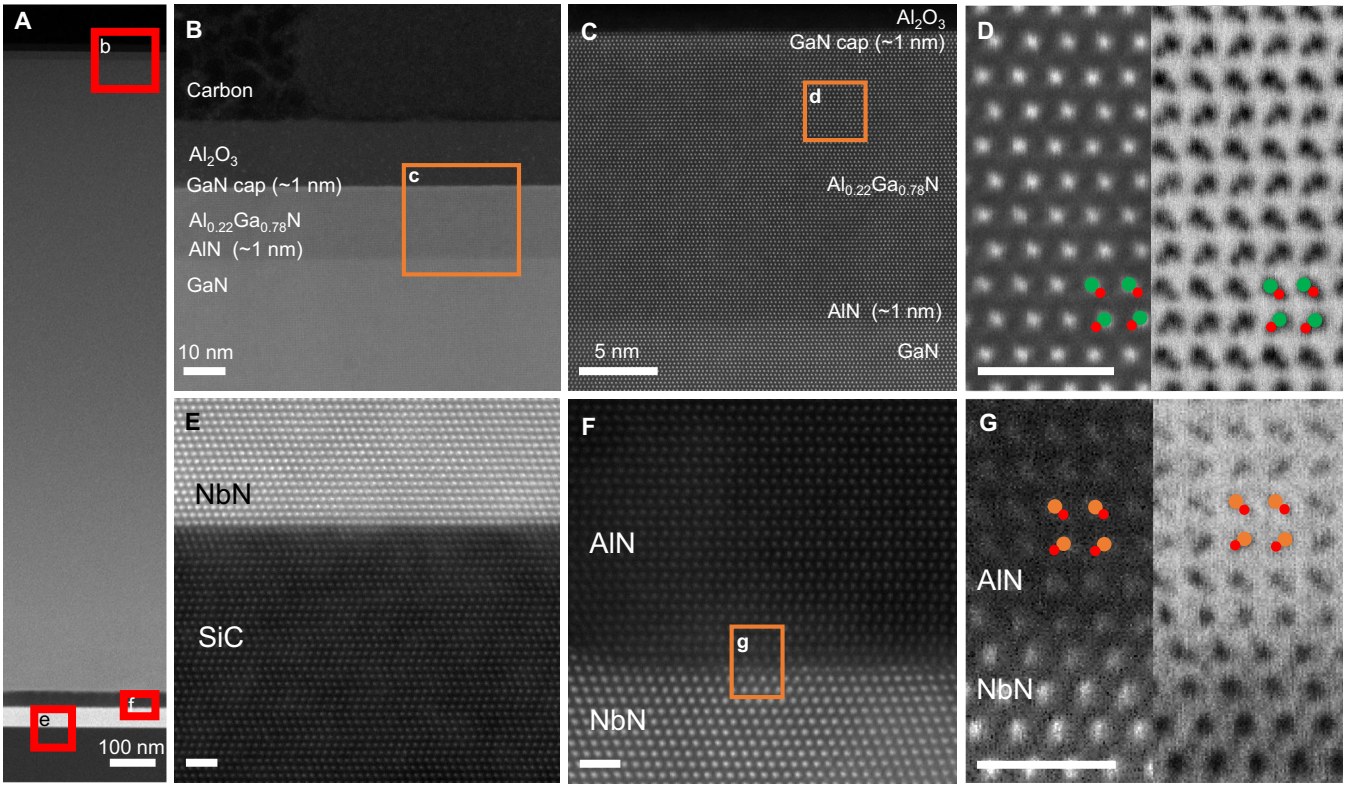

Fig. 1. TEM images of the epitaxial nitride heterostructure. (**A**) The overall structure of the GaN HEMT on NbN with protective carbon on top. (**B**) Enlargement of an area on the top as depicted in (A). The GaN cap and AlN layers have a slight change of contrast with respect to $Al_{0.22}Ga_{0.78}N$. (**C**) Atomically well-arranged lattice showing the high quality of the GaN HEMT. The boxed area in (C) is imaged in both high-angle annular dark field (HAADF) STEM (left) and annular bright field (ABF) STEM (right) images as in (**D**), which shows the Ga-polar structure of $Al_{0.22}Ga_{0.78}N$. The HAADF emphasizes the heavier atoms, while the ABF shows both. The labeled green atoms correspond to Ga, while red atoms correspond to N. (**E**) and (**F**) show the interfaces of NbN/SiC and AlN/NbN, respectively, which are located at the lower part of the GaN HEMT. (**G**) shows the Al-polar AlN crystal structure from the boxed region in (F). Orange atoms correspond to Al. The scale bars are 1 nm unless otherwise noted.

layer and is locked for all subsequent layers. This is evidenced by Fig. 1 (F and G), where we can see that the AlN nucleation layer is metal polar starting from the first layer grown on NbN. Therefore, our growth method has the ability to control the polarity of the nitride heterostructure on top of NbN and enables precise engineering of the location of the 2DEG.

The inset of Fig. 2A shows the epitaxial semiconductor/superconductor heterostructure. The NbN layer is grown by molecular beam epitaxy (MBE), and the GaN heterostructure, in which the 2DEG is formed at the heterojunction quantum well, is grown by MOCVD—the industrial tool for the production of nitride photonic and electronic devices in large scale. Further details of the growth procedure are provided in Materials and Methods. The epitaxial structure is then processed into a HEMT with a metal/oxide gate stack and ohmic source and drain contacts. The transistor exhibits switching, gain, and gate control of the 2DEG channel, as shown in the Supplementary Materials. The measured Hall-effect transport properties of the 2DEG channel at zero gate voltage indicates a density of $6.7 \times 10^{12}/cm^2$ and a mobility of 1600 $cm^2/V{\cdot}s$ at room temperature, which respectively become $6.5 \times 10^{12}/cm^2$ and 6100 $cm^2/V{\cdot}s$ at 390 mK. The increase in electron mobility at low temperature is due to the freeze-out of optical phonon scattering and is limited by the combination of dislocation scattering and interface roughness scattering. Interface roughness scattering is reduced at lower 2DEG densities: When the 2DEG density is lowered with the gate voltage, the low-temperature mobility increases to ~8500 $cm^2/V{\cdot}s$ before the crossover to dislocation scattering limit (see Materials and Methods and the Supplementary Materials for more details and a theoretical model). The near temperature independence of the 2DEG density is characteristic of 2DEGs formed by polarization-induced doping.

Figure 2A shows the longitudinal and transverse magnetoresistance R_{xx} and R_{xy} of the 2DEG measured in a gated Hall bar at 45 T and 390 mK. The $n = 1, 2, \ldots$ IQHE plateaus are clearly resolved in the Hall resistance R_{xy}, accompanied by the vanishing of the longitudinal magnetoresistance R_{xx} when the Fermi level is in the gap between Landau levels, the hallmark of the quantum Hall-insulating phase. The transition between the plateaus of the QHE states is accompanied by peaks in the R_{xx} when the Fermi level is located inside a Landau level. The lower gray region of Fig. 2B shows the range of temperatures and perpendicular magnetic fields over which the 50-nm epitaxial NbN layer remains superconducting, even after the deposition of the entire GaN/Al(Ga)N heterostructure by MOCVD and the subsequent processing of the HEMT device. The T_c is 16.5 K with a sharp transition of $\Delta T = 0.16$ K in width (see Materials and Methods), and the maximum out-of-plane H_c is 17.8 T (the in-plane value is 22.8 T).

Figure 2C shows that at magnetic fields as low as $B = 15$ T, the QHE plateaus, namely, $n = 4$ and 6 are resolved. While Fig. 2 (A and C) shows the magnetoresistance at a fixed B field and varying 2DEG

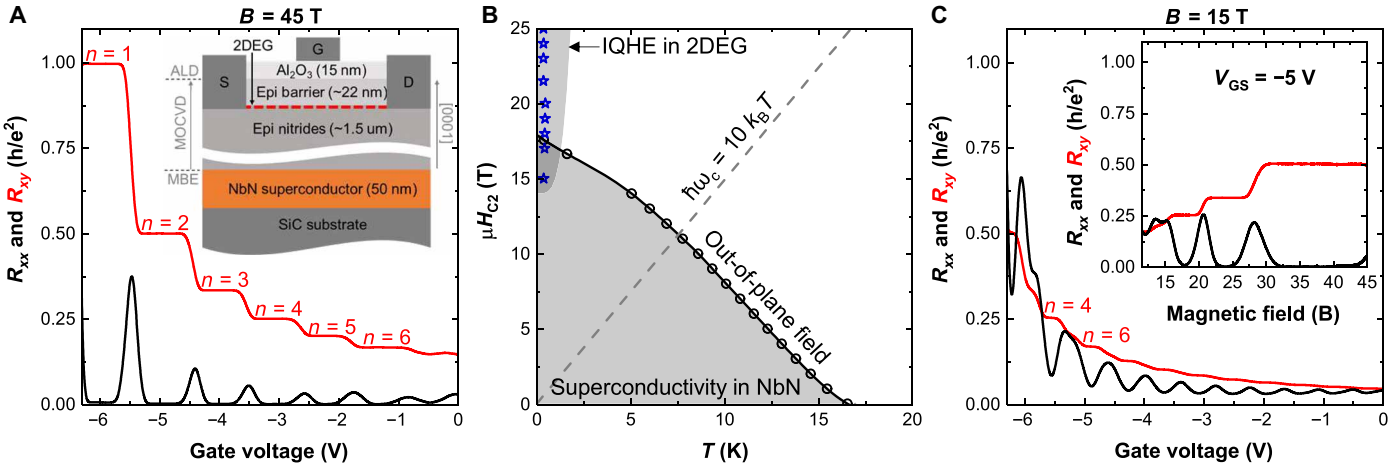

Fig. 2. Concurrence of the IQHE and superconductivity in an epitaxial nitride heterostructure. Measurements were taken at $T = 390$ mK. (**A**) R_{xy} (red) and R_{xx} (black) measurements taken at a magnetic field of 45 T for varying gate voltages of a gated Hall bar. Clear integer quantum Hall plateaus are observed. The inset shows the layer structure of the epitaxial semiconductor/superconductor heterostructure. The red dashed line shows the location of the 2DEG in the quantum well formed in the metal-polar heterostructure. (**B**) Out-of-plane magnetic field versus temperature phase space, where the black circles represent the superconductor to normal metal phase transition in the superconducting epitaxial NbN layer, and the blue stars indicate the IQHE in the epitaxial 2DEG. The shaded regions are to emphasize the overlap region where superconductivity and IQHE simultaneously occur in the heterostructure. The gray dashed line is given by $\hbar\omega_c = 10k_BT$, above which the IQHE is expected to be easily resolved for heterostructures with lower 2DEG densities and higher mobilities. (**C**) R_{xy} (red) and R_{xx} (black) measurements taken at a magnetic field of 15 T while the gate voltage is swept. At 15 T, initial indications of the IQHE are observed, especially at the fourth and sixth Landau levels. The inset shows the IQHE when the gate voltage is fixed at −5 V and magnetic field is swept.

density, the inset of Fig. 2C shows the resistances at fixed 2DEG density with varying perpendicular magnetic field. Clear QHE plateaus in R_{xy} accompanied by a vanishing R_{xx} are observed starting at $B \sim 15$ T, indicating the concurrent superconductivity and QHE phases. The regime of temperatures and magnetic fields in which the IQHE is seen in the 2DEG is shown in the upper gray region in Fig. 2B, indicating the overlapping region with superconductivity. The dashed line indicates the contour $\hbar\omega_c = 10k_BT$, the upper left part of which is the phase space for sufficient separation of the Landau levels to observe IQHE by simultaneously avoiding thermal and scattering related broadenings. For this study, superconductivity and IQHE are concurrent for $T < 1$ K and $\mu H < 18$ T, and the dashed line serves as a bound for possible IQHE occurrence with increases in 2DEG mobility.

Figure 3A shows the spectral plot of the measured R_{xy} versus magnetic field B and gate voltage V_{gs} measured at 390 mK. Figure 3B shows the corresponding R_{xx}. The integer quantum Hall steps are clearly resolved over a wide range of gate voltages, offering a rich palette of electronic states with varying topological indices. The values of the R_{xx} are either zero or low, except at the interplateau transitions of R_{xy}. From the slopes of the spectral plots, we extract the gate capacitance to be $C_{gs} \sim 149$ nF/cm^2, and the 2DEG density varies from less than 1.1×10^{12}/cm^2 to 6.7×10^{12}/cm^2 when the gate voltage is varied over -6.3 V $< V_{gs} < 0$ V. The conduction band-edge electron effective mass, which was extracted from temperature-dependent Shubnikov–de Haas oscillation amplitudes, is $m_c^* = (0.204 \pm 0.005)\, m_e$, where m_e is the free electron mass. The Landau levels are found to be spin-split with a magnetic field–dependent effective g factor with a maximum value of $g \sim 4.6$ (see Materials and Methods), which differs from the low magnetic field limit of $g_0 = 2$ (*7*). Enhancement of the g factor in low Landau level index is a well-known phenomenon in semiconductor 2DEGs (*8*, *9*). At large magnetic fields, when the Landau level spin-splitting is larger than the broadening due to disorder, the population of up- and down-spins varies greatly. Up- and down-spin electrons then experience different exchange interactions. This enhancement is largest when the chemical potential is between spin-resolved Landau levels (of even and odd index) and minimal when the chemical potential is between orbitally resolved Landau levels (odd and even index).

The Landau fan plots and the direct measurement of the 2DEG densities versus the gate voltage corroborate the 2DEG density obtained from the Hall-effect measurement at low B fields (see the Supplementary Materials). The Hall coefficients indicate electron mobilities ranging from $1200 < \mu_H < 8500$ cm^2/V·s at 390 mK over the range of 2DEG densities. While the mobilities are smaller than narrower-gap GaAs-based heterostructures, it is of the same order as silicon MOSFET 2DEGs in which the IQHE was observed for the first time (*1*). However, it should not be perceived as a limit of the GaN 2DEGs. From a theoretical model discussed in Materials and Methods, we have evaluated the mobility limiting scattering mechanisms (*10*, *11*), which indicate that the measured values are limited by Coulomb scattering from threading dislocations and/or background impurities at low 2DEG densities, and by interface roughness scattering at higher densities, which occurs when the 2DEG wave function samples thickness variations as small as a monolayer of the AlN/GaN heterojunction. The electron mobility at low 2DEG densities in GaN/AlGaN heterostructures can reach ~50,000 to 170,000 cm^2/V·s with lowering of the dislocation density and background impurities (*12*–*16*). In such higher mobility 2DEGs, the IQHE should be observed in a far wider window than seen here, expanding into the top left region of the dashed contour in Fig. 2B. Therefore, improvements to the GaN/AlGaN heterostructures can significantly increase the physical parameter space over which the IQHE and superconductivity can coexist. Filling this space will create an attractive epitaxial platform for the study and use of topologically protected transport while taking advantage of the many

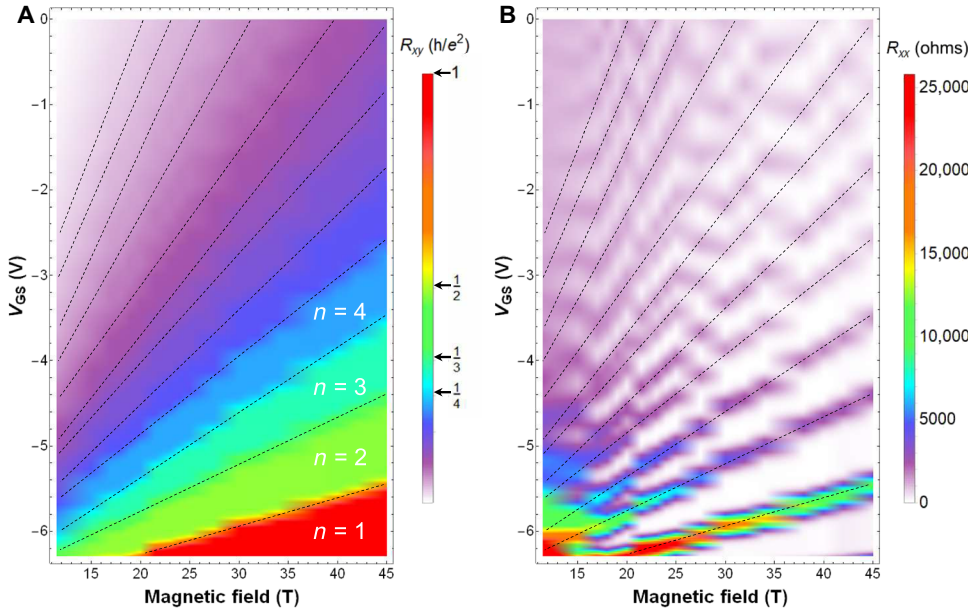

Fig. 3. Color density plots of the measured R_{xy} and R_{xx} of the GaN 2DEG. The (**A**) R_{xy} and (**B**) R_{xx} plots were generated from a linear interpolation of experimental gate-voltage sweep measurements taken at fixed magnetic fields (see fig. S3 for a set of curves representing of the measurements). All data were measured at 390 mK. The black dotted lines are meant to guide the eye along transitions between Landau levels.

electronic and photonic possibilities offered by the nitride semiconductor system.

DISCUSSION

The coexistence of superconductivity and the 2DEG IQHE in an epitaxial superconductor/semiconductor heterostructure signals several new possibilities. In this work, the GaN 2DEG heterostructure is grown on top of a highly crystalline epitaxial NbN layer with high T_c and H_c. The GaN system has the advantage of having demonstrated among the lowest contact resistances of all semiconductors (*17*). These low contact resistances are achieved by using regrown n-GaN and Ti metal (*18*–*20*). The diffusion of N atoms at the n-GaN/Ti interface results in a highly doped subcontact region and creates TiN, which itself forms an ohmic contact with GaN (*21*). A previous work that used Nb-Ti/Al/Ni/Au contacts to a GaN 2DEG attributed the low resistance of the contacts to NbN formation (*22*). Building on the GaN regrown ohmic contact process used in HEMTs (*18*–*20*), it may be possible to grow NbN in the source/drain regions of the transistor or in the ohmic contact regions of gated Hall bars. In such a structure, the NbN can remain superconducting when the gate voltage, assisted by a magnetic field, puts the 2DEG into an IQHE state. This will allow the direct injection of Cooper pairs into IQHE edge states. Very nice demonstrations of this phenomenon have previously been done, typically with nonepitaxial structures using sputtered Nb, NbN, or MoRe (*23*–*29*). While these works have shown high-quality and transparent interfaces, epitaxial structures can be additionally advantageous because of their excellent scalability, higher crystalline quality, and lower interfacial impurities that can impede phase-coherent transport (*30*, *31*). Epitaxy also enables vertical integration because additional epitaxial materials, including semiconductors for transistors, can be grown on top of the semiconductor/superconductor system. Other works that use epitaxial semiconductor/superconductor integration have shown promising results with Al superconductors grown on InGaAs/InAs 2DEGs (*32*, *33*). However, the critical magnetic field and temperature of Al is quite low and motivates the search for other superconductor/semiconductor combinations (*34*). Our demonstration of the large critical field of NbN and its epitaxial integration with nitride semiconductors makes nitride heterostructures promising for further research. Furthermore, the vertical integration enabled by epitaxy and the 2DEG location engineering enabled by polarity control in the nitride heterostructures allows for more geometries and flexibility in future devices.

The success of Cooper pair injection would require low barrier contacts at the edges, something that was previously achieved in nitrides by regrowth using n+ GaN (*17*, *20*) but needs to be proven for the NbN/2DEG HEMT interface. Because the 2DEG is formed by polarization-induced doping instead of modulation doping, it is unaffected by random dopant fluctuations of modulation doped heterostructures. This will ensure that very thin lithographically defined gated fins, which are controlled quantum wires, can allow 1D transport in the longitudinal direction. Combined with the Rashba effect due to spontaneous and piezoelectric polarization (*35*) and the high crystalline quality of the epitaxial interfaces, Majorana Fermion modes with gate-controlled braiding could potentially be realized in these heterostructures. These possibilities, combined with the rapid wafer-scale material perfection achieved by growth and the processing advances of the nitride semiconductor material system due to its rapidly increasing importance in electronics and photonics, make the NbN/GaN superconductor/semiconductor system of unique and high interest for future quantum devices.

MATERIALS AND METHODS

Heterostructure growth

The 50-nm-thick NbN layer was grown epitaxially by plasma-assisted MBE on a 3-inch-diameter semi-insulating Si-face 6H-SiC wafer that

was chemical-mechanically polished to an epi-ready finish using equipment and methods discussed previously (*5*). Atomic force microscopy measurements revealed that the NbN film had an root mean square roughness of approximately 0.9 nm after growth.

As shown in fig. S1A, a ~20-nm high-temperature AlN nucleation layer was then deposited on top of the MBE-grown NbN by MOCVD, followed by a 1.5-μm GaN buffer layer. Last, an AlN spacer/AlGaN barrier/GaN cap layers were deposited. After epitaxial growth, wet chemical etching by potassium hydroxide solution was used to verify that the epi film has a metal polarity. Capacitance-voltage profiling with a mercury probe confirmed the formation of 2DEG at the AlGaN/AlN/GaN heterojunction.

Fabrication of devices

The HEMT devices were fabricated starting with Ti/Al/Ni/Au (20/200/40/50 nm) ohmic contacts annealed at 800°C for 30 s under a N_2 atmosphere providing a measured contact resistance of 0.75 ohm·mm. Mesa isolation was then performed by etching through the AlGaN barrier using a Cl_2/BCl_3-based plasma etch. To reduce gate leakage current, a 15-nm Al_2O_3 gate insulator was deposited by thermal atomic layer deposition at 250°C. The Al_2O_3 was removed from above the ohmic contacts using an hydrofluoric acid (HF)–based wet etch. Last, gates and probe pads were defined via a Pt/Au (20/300 nm) metallization. Figure S1B shows a scanning electron microscopy image of the finished gated Hall bar (GHBAR) used for the IQHE measurements.

Device characteristics

The device characteristics of the gated Hall bars contacted to the 2DEG are shown in fig. S2. The I_d versus V_{ds} and I_d versus V_{gs} show good transistor behavior with >2 orders of current modulation, despite the very large area of the gates. The gate leakage current becomes comparable to the channel current at $V_{gs} \sim -8$ V, which is a lower gate voltage than our analysis in the range $-6.5\ \text{V} < V_{gs} < 0\ \text{V}$. The capacitance-voltage measurement shows the depletion of the 2DEG. The hysteresis in the curves is attributed to slow trap states in the GaN buffer and/or the Al_2O_3 gate dielectric.

Magnetotransport measurements

Resistivity and Hall-effect measurements were taken on a gated Hall bar device (shown in fig. S1B) that was contacted to the GaN 2DEG and separated from the NbN buried layer by the insulating nitride layers. The measurements were taken in a hybrid superconductor/resistive magnet up to 45 T and at temperatures as low as 350 mK. Figure S3 shows stacked plots of the raw Hall effect and resistivity measurements when gate voltage was varied and magnetic field was fixed. In total, data were taken at magnetic fields of 11.5, 15, 17, 18, 19, 20, 21.5, 23, 24, 25, 27.5, 30, 32, 34, 38, 40, 42, and 45 T, and each magnetic field represents a vertical slice of Fig. 3. The peaks of the Shubnikov–de Haas oscillations in resistivity were plotted as a function of $1/B$ to obtain the Landau fan plot shown in fig. S4, which indicates that the IQHE regime is reached. The g factor of the 2DEG was calculated using $g = \frac{2m_e}{m_e^*}\left(\frac{1/H_N^+ - 1/H_N^-}{\delta/H}\right)$, where m_e^* is the effective electron mass, H_N^+ and H_N^- are the magnetic field positions of the spin-split R_{xx} peaks, and δ/H is the period of the R_{xx} oscillations (*36*). The spin-split peak positions were obtained using Gaussian fits to our R_{xx} versus B data, as shown in fig. S5. We obtain g factors of 2.7 to 2.8 at intermediate magnetic fields (13 to 18 T) and 4.5 to 4.6 at high magnetic fields (28 to 41 T). The g factors were extracted using two different gate voltages, which resulted in different Landau levels at similar magnetic fields. Despite the change in Landau levels, the g factors were quite consistent at similar magnetic fields. Therefore, we conclude that the g factor of the 2DEG increases with magnetic field.

Magnetotransport measurements of the buried NbN layer above 2 K in temperature and below 14 T in magnetic field were conducted in a quantum design physical property measurement system (PPMS). The NbN was contacted by using indium dots that ran along the sides of the entire structure. For this reason, the raw resistance measurements, shown in fig. S6, include contributions from the semiconducting layers and do not drop all the way down to zero. The superconducting critical temperature at each magnetic field was determined by electrical resistance measurements (shown in fig. S6) and defined as the temperature where resistance of NbN was 50% of the normal metal resistance. The superconducting transition width, $\Delta T = 0.16$ K, was defined as the temperature difference between resistances 90 and 10% of the normal metal resistance, that is, $\Delta T = T_c^{90\%} - T_c^{10\%}$. For the resistance measurement at zero magnetic field in fig. S7, we used contacts that had the 2DEG between them etched away. The isolated contacts were then used to electrically break down the nitride layers over the NbN layer and subsequently used for four-wire resistance measurements, which negated any contribution from the semiconducting layers.

Transmission electron microscopy

Cross-sectional TEM specimen was prepared using a Thermo Helios G4 UX Focused Ion Beam (FIB) with a final milling voltage of 5 keV to reduce damage. The sample surface was protected from ion-beam damage by carbon and platinum deposited layers. The sample was then examined by STEM using an aberration-corrected Titan Themis operating at 300 keV.

Energy band diagrams

Figure S8 shows the energy band diagram of the gated heterostructure in which the 2DEG exhibiting IQHE is formed. The energy band diagram is calculated by self-consistently solving the effective-mass Schrodinger equation and the Poisson equation using the software 1D Poisson (available from https://www3.nd.edu/~gsnider/). The epitaxial growth creates a metal-polar crystal of GaN/AlN/AlGaN, with the growth in the 0001 direction of the wurtzite lattice from the right toward the surface on the left. This crystal orientation is opposite to what was first realized in (*5*). As a result, in (*5*), the 2DEG was formed in the top AlGaN/GaN heterojunction, whereas in this structure, it is formed at the bottom AlN/GaN heterojunction as seen in the figure. The 2DEG is located in the triangular quantum well as indicated, due to the polarization discontinuity and the large conduction band offset between AlN and GaN. The profile of the 2DEG is proportional to the squared wave function, which is seen to decay in the thin 1-nm AlN layer before reaching the AlGaN layer. The large conduction band offset barrier limits the electron wave function penetration into the AlN layer and prevents it from reaching the AlGaN layer. Because the AlGaN layer is a random alloy, this scheme avoids incurring another penalty in alloy scattering. The scattering mechanisms are shown in fig. S9.

Mobility of the GaN 2DEG

Figure S9 shows the measured and calculated electron mobilities of the 2DEG that exhibits IQHE. The figure on the left shows the measured

room temperature mobility of ~1600 $cm^2/V{\cdot}s$ and a 0.4 K mobility of 6100 $cm^2/V{\cdot}s$ and the corresponding theoretical model in solid lines. The room temperature mobility is limited by polar optical phonon scattering, and the low-temperature mobility is limited by interface roughness scattering at the 2DEG density of ~$6.5 \times 10^{12}/cm^2$; at this density dislocation, scattering is efficiently screened. The figure on the right shows the measured low-temperature mobility for varying 2DEG density, and the solid theoretical lines are from the same model as the left figure. When the 2DEG density is decreased with the gate voltage, the centroid of the 2DEG wave function moves away from the AlN/GaN heterojunction, reducing interface roughness scattering. However, because of insufficient screening of the Coulomb potential of charged dislocations at lower 2DEG densities, dislocation density dominates scattering, switching roles with interface roughness scattering. Though the model predicts a slightly higher mobility than what is measured at the lowest 2DEG densities, the same model effectively explains the experimental data. Alloy scattering is avoided because of the presence of the 1-nm AlN interlayer that prevents the wave function of the 2DEG from experiencing alloy disorder scattering from AlGaN, as was indicated in fig. S8.

The theoretical model used can be found in chapter 4 of (*6*). As a brief summary for the low-temperature scattering mechanisms, the mobility is related to the momentum scattering rate via $\mu = q\langle\tau\rangle/m^*$, where q is the electron charge, m^*~0.2 m_e is the conduction band electron effective mass in GaN, and $\langle\tau\rangle$ is the ensemble averaged value of the momentum scattering time. The momentum scattering rate is given by the Fermi golden rule $1/\tau = (2\pi/\hbar)\,|\,W_{if}\,|^2\delta(E_i - E_f)$, where $\hbar$ is the reduced Planck's constant, E_i and E_f are the initial and final electron energies, $\delta(\ldots)$ is the Dirac delta function, and $|\,W_{if}\,|^2$ is the square of the matrix element of the perturbation potential that causes electron scattering. For dislocation scattering, the perturbation is the Coulomb potential of a line charge that is perpendicular to the plane of the 2DEG. For the model presented here, the dislocation density used is $2 \times 10^9/cm^2$ and a filling factor of 1, meaning there is one charge per unit cell in the 0001 direction of the crystal. For interface roughness scattering, the electron experiences a spatially varying quantum well width due to one to two monolayer variations in the AlN/GaN heterojunction because the interface is not atomically abrupt. This variation is captured by a height of $\Delta \sim 5$ Å and a lateral correlation length of $L \sim 13$ Å. The final matrix element takes the form of a Gaussian of these two parameters and is a well-established model for transport of 2DEGs at several heterointerfaces such as Si MOSFETs, InSb, GaAs, and GaN heterostructures.

SUPPLEMENTARY MATERIALS

Supplementary material for this article is available at http://advances.sciencemag.org/cgi/content/full/7/8/eabf1388/DC1

REFERENCES AND NOTES

1. K. v. Klitzing, G. Dorda, M. Pepper, New method for high-accuracy determination of the fine-structure constant based on quantized Hall resistance. *Phys. Rev. Lett.* **45**, 494–497 (1980).
2. D. J. Thouless, M. Kohmoto, M. P. Nightingale, M. den Nijs, Quantized Hall conductance in a two-dimensional periodic potential. *Phys. Rev. Lett.* **49**, 405–408 (1982).
3. J. Clarke, F. K. Wilhelm, Superconducting quantum bits. *Nature* **453**, 1031–1042 (2008).
4. B. N. Taylor, New measurements standards for 1990. *Phys. Today* **42**, 23–26 (1989).
5. R. Yan, G. Khalsa, S. Vishwanath, Y. Han, J. Wright, S. Rouvimov, D. Scott Katzer, N. Nepal, B. P. Downey, D. A. Muller, H. G. Xing, D. J. Meyer, D. Jena, GaN/NbN epitaxial semiconductor/superconductor heterostructures. *Nature* **555**, 183–189 (2018).
6. C. Wood, D. Jena, *Polarization Effects in Semiconductors* (Springer US, 2008).
7. W. E. Carlos, J. A. Freitas Jr., M. A. Khan, D. T. Olson, J. N. Kuznia, Electron-spin-resonance studies of donors in wurtzite GaN. *Phys. Rev. B* **48**, 17878–17884 (1993).
8. T. Ando, Y. Uemura, Theory of oscillatory g factor in an MOS inversion layer under strong magnetic fields. *J. Phys. Soc. Jpn.* **37**, 1044–1052 (1974).
9. N. Tang, K. Han, F.-C. Lu, J.-X. Duan, F.-J. Xu, B. Shen, Exchange enhancement of spin-splitting in $Al_xGa_{1-x}N$/GaN heterostructures in tilted magnetic fields. *Chin. Phys. Lett.* **28**, 037103 (2011).
10. D. Jena, I. Smorchkova, A. C. Gossard, U. K. Mishra, Electron transport in III-V nitride two-dimensional electron gases. *Phys. Status Solidi B* **228**, 617–619 (2001).
11. D. Jena, U. K. Mishra, Quantum and classical scattering times due to charged dislocations in an impure electron gas. *Phys. Rev. B* **66**, 241307(R) (2002).
12. M. J. Manfra, L. N. Pfeiffer, K. W. West, H. L. Stormer, K. W. Baldwin, J. W. P. Hsu, D. V. Lang, R. J. Molnar, High-mobility AlGaN/GaN heterostructures grown by molecular-beam epitaxy on GaN templates prepared by hydride vapor phase epitaxy. *Appl. Phys. Lett.* **77**, 2888–2890 (2000).
13. M. J. Manfra, K. W. Baldwin, A. M. Sergent, R. J. Molnar, J. Caissie, Electron mobility in very low density GaN/AlGaN/GaN heterostructures. *Appl. Phys. Lett.* **85**, 1722–1724 (2004).
14. M. J. Manfra, K. W. Baldwin, A. M. Sergent, K. W. West, R. J. Molnar, J. Caissie, Electron mobility exceeding 160000 cm^2/Vs in AlGaN/GaN heterostructures grown by molecular-beam epitaxy. *Appl. Phys. Lett.* **85**, 5394–5396 (2004).
15. C. Skierbiszewski, K. Dybko, W. Knap, M. Siekacz, W. Krupczynski, G. Nowak, M. Bockowski, J. Lusakowski, Z. R. Wasilewski, D. Maude, T. Suski, S. Porowski, High mobility two-dimensional electron gas in AlGaN/GaN heterostructures grown on bulk GaN by plasma assisted molecular beam epitaxy. *Appl. Phys. Lett.* **86**, 102106 (2005).
16. S. Schmult, M. J. Manfra, A. M. Sergent, A. Punnoose, H. T. Chou, D. Goldhaber-Gordon, R. J. Molnar, Quantum transport in high mobility AlGaN/GaN 2DEGs and nanostructures. *Phys. Status Solidi B* **243**, 1706–1712 (2006).
17. D. Jena, K. Banerjee, G. H. Xing, 2D crystal semiconductors: Intimate contacts. *Nat. Mater.* **13**, 1076–1078 (2014).
18. J. Guo, Y. Cao, C. Lian, T. Zimmermann, G. Li, J. Verma, X. Gao, S. Guo, P. Saunier, M. Wistey, D. Jena, H. Xing, Metal-face InAlN/AlN/GaN high electron mobility transistors with regrown ohmic contacts by molecular beam epitaxy. *Phys. Status Solidi A* **208**, 1617–1619 (2011).
19. J. Guo, G. Li, F. Faria, Y. Cao, R. Wang, J. Verma, X. Gao, S. Guo, E. Beam, A. Ketterson, M. Schuette, P. Saunier, M. Wistey, D. Jena, H. Xing, MBE-regrown ohmics in InAlN HEMTs with a regrowth interface resistance of 0.05Ω-mm. *IEEE Electron Device Lett.* **33**, 525–527 (2012).
20. F. Afroz Faria, J. Guo, P. Zhao, G. Li, P. Kumar Kandaswamy, M. Wistey, H. Xing, D. Jena, Ultra-low resistance ohmic contacts to GaN with high Si doping concentrations grown by molecular beam epitaxy. *Appl. Phys. Lett.* **101**, 032109 (2012).
21. E. Kamińska, A. Piotrowska, M. Guziewicz, S. Kasjaniuk, A. Barcz, E. Dynowska, M. D. Bremser, O. H. Nam, R. F. Davis, Ohmic contact to n-GaN with TiN diffusion barrier. *MRS Proc.* **449**, 1055 (1996).
22. G. Vanko, T. Lalinský, Ž. Mozolová, J. Liday, P. Vogrinčič, A. Vincze, F. Uherek, Š. Haščík, I. Kostič, Nb-Ti/Al/Ni/Au based ohmic contacts to AlGaN/GaN. *Vacuum* **82**, 193–196 (2007).
23. P. Rickhaus, M. Weiss, L. Marot, C. Schönenberger, Quantum Hall effect in graphene with superconducting electrodes. *Nano Lett.* **12**, 1942–1945 (2012).
24. K. Komatsu, C. Li, S. Autier-Laurent, H. Bouchiat, S. Guéron, Superconducting proximity effect in long superconductor/graphene/superconductor junctions: From specular Andreev reflection at zero field to the quantum Hall regime. *Phys. Rev. B* **86**, 115412 (2012).
25. Z. Wan, A. Kazakov, M. J. Manfra, L. N. Pfeiffer, K. W. West, L. P. Rokhinson, Induced superconductivity in high-mobility two-dimensional electron gas in gallium arsenide heterostructures. *Nat. Commun.* **6**, 7426 (2015).
26. G.-H. Lee, K.-F. Huang, D. K. Efetov, D. S. Wei, S. Hart, T. Taniguchi, K. Watanabe, A. Yacoby, P. Kim, Inducing superconducting correlation in quantum Hall edge states. *Nat. Phys.* **13**, 693–698 (2017).
27. J. Zhi, N. Kang, F. Su, D. Fan, S. Li, D. Pan, S. P. Zhao, J. Zhao, H. Q. Xu, Coexistence of induced superconductivity and quantum Hall states in InSb nanosheets. *Phys. Rev. B* **99**, 245302 (2019).
28. V. E. Calado, S. Goswami, G. Nanda, M. Diez, A. R. Akhmerov, K. Watanabe, T. Taniguchi, T. M. Klapwijk, L. M. K. Vandersypen, Ballistic Josephson junctions in edge-contacted graphene. *Nat. Nanotechnol.* **10**, 761–764 (2015).
29. F. Amet, C. T. Ke, I. V. Borzenets, J. Wang, K. Watanabe, T. Taniguchi, R. S. Deacon, M. Yamamoto, Y. Bomze, S. Tarucha, G. Finkelstein, Supercurrent in the quantum Hall regime. *Science* **352**, 966–969 (2016).
30. P. Krogstrup, N. L. B. Ziino, W. Chang, S. M. Albrecht, M. H. Madsen, E. Johnson, J. Nygård, C. M. Marcus, T. S. Jespersen, Epitaxy of semiconductor-superconductor nanowires. *Nat. Mater.* **14**, 400–406 (2015).

31. S. D. Sarma, M. Freedman, C. Nayak, Majorana zero modes and topological quantum computations. *npq Quant. Inf.* **1**, 15001 (2015).
32. J. Shabani, M. Kjaergaard, H. J. Suominen, Y. Kim, F. Nichele, K. Pakrouski, T. Stankevic, R. M. Lutchyn, P. Krogstrup, R. Feidenhans'l, S. Kraemer, C. Nayak, M. Troyer, C. M. Marcus, C. J. Palmstrøm, Two-dimensional epitaxial superconductor-semiconductor heterostructures: A platform for topological superconducting networks. *Phys. Rev. B* **93**, 155402 (2016).
33. M. Kjaergaard, F. Nichele, H. J. Suominen, M. P. Nowak, M. Wimmer, A. R. Akhmerov, J. A. Folk, K. Flensberg, J. Shabani, C. J. Palmstrøm, C. M. Marcus, Quantized conductance doubling and hard gap in a two-dimensional semiconductor-superconductor heterostructure. *Nat. Commun.* **7**, 12841 (2016).
34. S. M. Frolov, M. J. Manfra, J. D. Sau, Topological superconductivity in hybrid devices. *Nat. Phys.* **16**, 718–724 (2020).
35. M. S. Miao, Q. Yan, C. G. Van de Walle, W. K. Lou, L. L. Li, K. Chang, Polarization-driven topological insulator transition in a GaN/InN/GaN quantum well. *Phys. Rev. Lett.* **109**, 186803 (2012).
36. G. A. Antcliffe, R. A. Straddling, De Haas-Shubnikov effect in In Sb with high electron concentrations. *Phys. Lett.* **20**, 119–121 (1966).
37. P. G. de Gennes, Behavior of dirty superconductors in high magnetic fields. *Phys. Kondens. Mater.* **3**, 79–90 (1964).
38. K. Maki, The magnetic properties of superconducting alloys I. *Physics* **1**, 21–30 (1964).
39. A. Godeke, M. C. Jewell, A. A. Golubov, B. Ten Haken, D. C. Larbalestier, Inconsistencies between extrapolated and actual critical fields in Nb_3Sn wires as demonstrated by direct measurements of H_{c2}, H^* and T_c. *Supercond. Sci. Technol.* **16**, 1019–1025 (2003).

Acknowledgments: We thank J. Wright for helpful discussions on the growth and characterization of NbN films and R. Yan, S. Bader, and A. Chaney for helpful discussions on the electrical characterization of the devices. **Funding:** This work was supported by the Office of Naval Research under grant no. N00014-17-1-2414 monitored by P. Maki and by the Cornell/AFOSR ACCESS center of excellence (FA9550-18-1-0529). The research was partially supported by the National Science Foundation under grant no. NewLAW EFMA 1741694, and P.D. was supported by the National Science Foundation Graduate Research Fellowship under grant no. DGE-1650441. The National High Magnetic Field Laboratory was supported by the National Science Foundation Cooperative agreement no. DMR-1644779 and the State of Florida. This work made use of a Helios FIB supported by NSF (DMR-1539918) and the Cornell Center for Materials Research shared facilities, which are supported through the NSF MRSEC program (DMR-1719875). **Author contributions:** P.D. performed electrical and magnetotransport measurements with help from A.S. C.S.C. performed TEM measurements and analysis under the guidance of D.A.M. D.S.K., N.N., B.P.D., V.D.W., and D.J.M. grew and characterized the NbN films and fabricated the devices. A.X., E.B., Y.C., and C.L. grew and characterized the AlN/AlGaN/GaN layers. P.D., G.K., and D.J. conducted experimental data analysis and theoretical calculations with help from H.G.X. P.D., G.K., and D.J. wrote the manuscript with input from all authors. **Competing interests:** G.K., H.G.X., D.J., D.S.K., N.N., B.P.D., and D.J.M. are inventors on a patent application related to this work filed by Cornell University and U.S. Naval Research Laboratory Tech Transfer (no. WO 2019/173448 A1, filed 6 March 2019, published 12 September 2019). The authors declare that they have no other competing interests. **Data and materials availability:** All data needed to evaluate the conclusions in the paper are present in the paper and/or the Supplementary Materials. Additional data related to this paper may be requested from the authors.

Submitted 12 October 2020
Accepted 6 January 2021
Published 19 February 2021
10.1126/sciadv.abf1388

Citation: P. Dang, G. Khalsa, C. S. Chang, D. S. Katzer, N. Nepal, B. P. Downey, V. D. Wheeler, A. Suslov, A. Xie, E. Beam, Y. Cao, C. Lee, D. A. Muller, H. G. Xing, D. J. Meyer, D. Jena, An all-epitaxial nitride heterostructure with concurrent quantum Hall effect and superconductivity. *Sci. Adv.* **7**, eabf1388 (2021).

An all-epitaxial nitride heterostructure with concurrent quantum Hall effect and superconductivity

Phillip Dang, Guru Khalsa, Celesta S. Chang, D. Scott Katzer, Neeraj Nepal, Brian P. Downey, Virginia D. Wheeler, Alexey Suslov, Andy Xie, Edward Beam, Yu Cao, Cathy Lee, David A. Muller, Huili Grace Xing, David J. Meyer and Debdeep Jena

Sci Adv **7** (8), eabf1388.
DOI: 10.1126/sciadv.abf1388

Science Advances
AAAS

advances.sciencemag.org/cgi/content/full/7/8/eabf1388/DC1

Supplementary Materials for

An all-epitaxial nitride heterostructure with concurrent quantum Hall effect and superconductivity

Phillip Dang*, Guru Khalsa*, Celesta S. Chang, D. Scott Katzer, Neeraj Nepal, Brian P. Downey, Virginia D. Wheeler, Alexey Suslov, Andy Xie, Edward Beam, Yu Cao, Cathy Lee, David A. Muller, Huili Grace Xing, David J. Meyer, Debdeep Jena*

*Corresponding author. Email: pd382@cornell.edu (P.D.); gsk63@cornell.edu (G.K.); djena@cornell.edu (D.J.)

Published 19 February 2021, *Sci. Adv.* **7**, abf1388 (2021)
DOI: 10.1126/sciadv.abf1388

This PDF file includes:

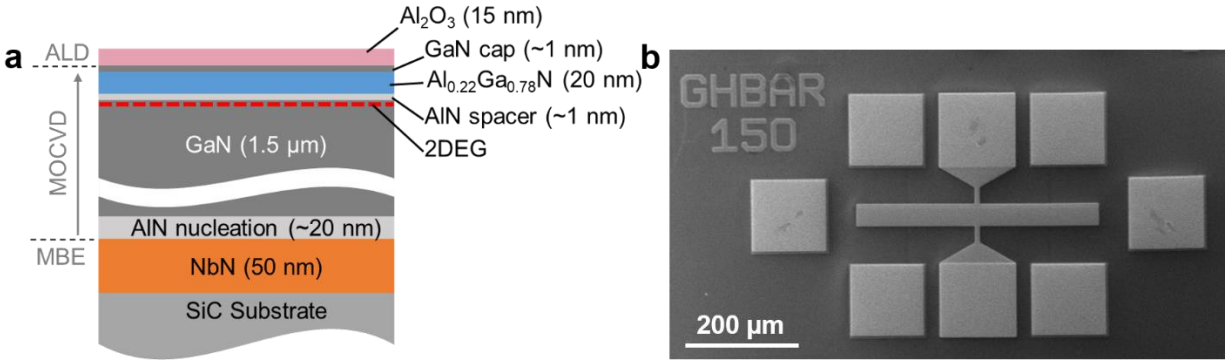

Fig. S1. Images of the sample measured. (a) The layer structure of the device in which the measurements were performed. (b) Scanning electron microscope image of the gated Hall bars used to measure R_{xx} and R_{xy}. The Hall bar is a 250 μm × 20 μm rectangle, and the voltage pads are longitudinally 150 μm apart.

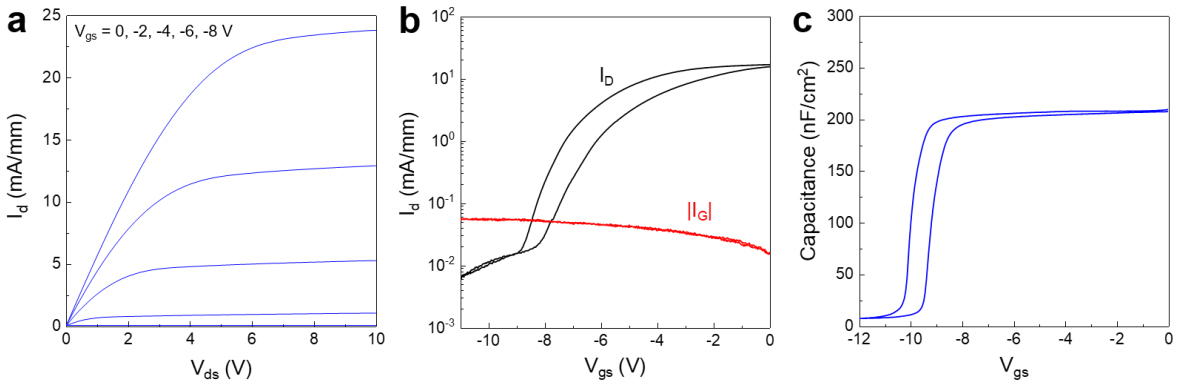

Fig. S2. Device characteristics of the gated GaN 2DEG. (a) I_d vs. V_{ds} of a gated Hall bar showing good transistor behavior despite the very large gate area. (b) I_d vs. V_{gs} of a gated Hall bar showing ~3 orders of current modulation and gate leakage currents that are low when $V_{gs} > -7$ V, the regime of interest in the IQHE measurements. (c) Capacitance vs. V_{gs} measurement of a diode showing depletion of the carriers.

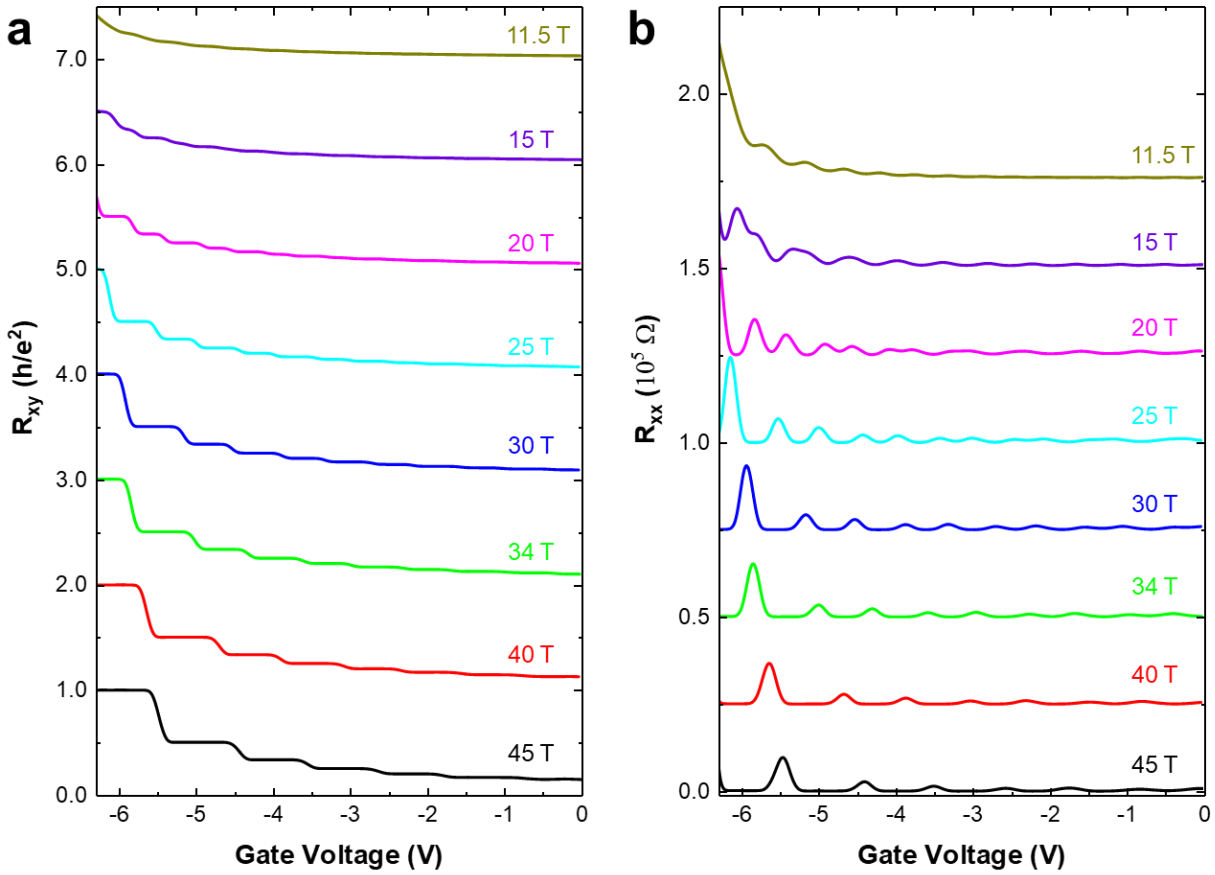

Fig. S3. Stacked plots of R_{xy} and R_{xx} versus gate voltage at various magnetic fields. (a) is R_{xy}, and (b) is R_{xx}. Each R_{xy} curve is shifted by h/e^2 from the zero of the curve underneath, and each R_{xx} curve is shifted by 25000 Ω from the zero of the curve underneath This is a representative set of data used to create Figure 3 (each line represents a vertical slice in Figure 3). In total, data was taken at magnetic fields of 11.5, 15, 17, 18, 19, 20, 21.5, 23, 24, 25, 27.5, 30, 32, 34, 38, 40, 42, and 45 T. All data was taken at 390 mK.

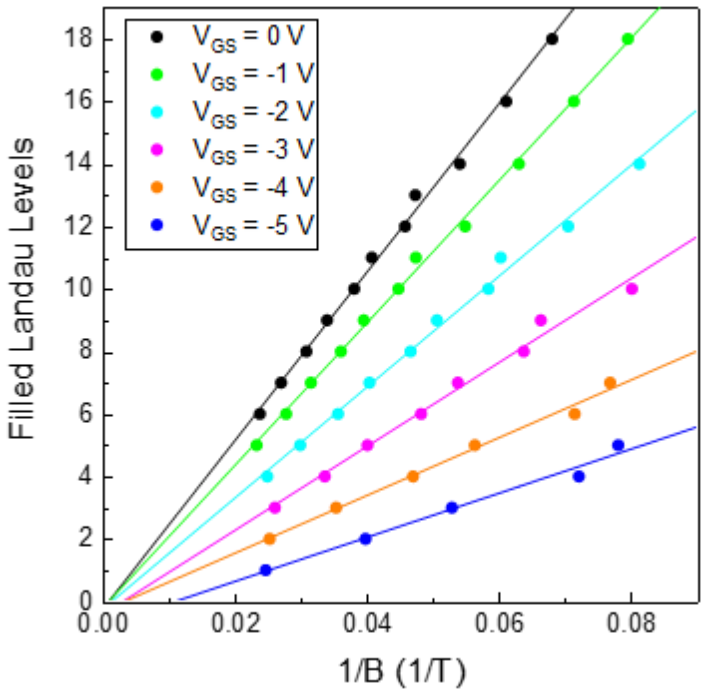

Fig. S4. Landau fan diagram extracted from the R_{xx} oscillation maxima. The 1st Landau level is reached by depleting the 2DEG with the gate voltage.

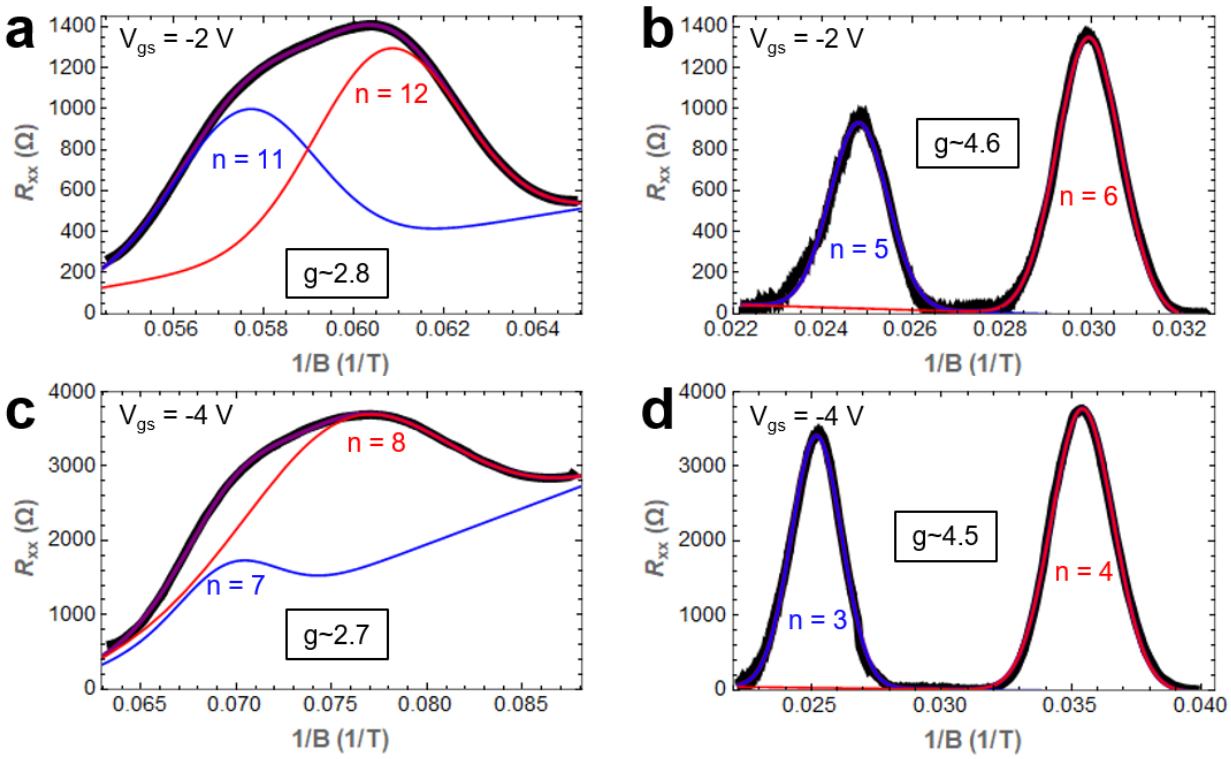

Fig. S5. Fits of R_{xx} vs. $1/B$ oscillation peaks that were used to extract the g-factors of the 2DEG. The black lines are experimental data, the purple lines are fits to the data using a sum of Gaussians, and the blue and red lines are Gaussian fits to the individual spin-split peaks. A gate voltage of -2 V was used so that we could resolve the spin-split peaks at both (a) intermediate magnetic fields of 16.4 - 17.4 T and (b) high magnetic fields of 33.4 - 40.4 T. These peaks respectively correspond to (a) the n = 11, 12 and (b) the n = 5, 6 Landau levels and resulted in g-factors of (a) ~2.8 and (b) ~4.6. To see if the g-factor values were consistent, we used a gate voltage of -4 V to obtain (c) the n = 7, 8 and (d) the n = 3, 4 Landau levels at magnetic fields similar to (a) and (b), respectively. The resulting g-factors were (c) ~2.7 and (d) ~4.5.

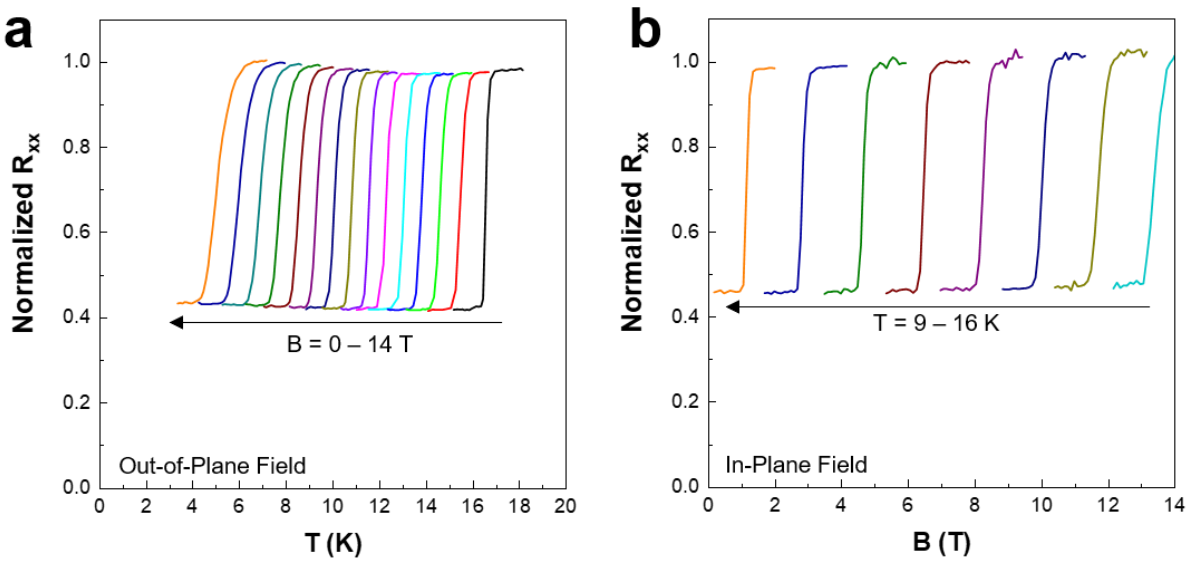

Fig. S6. Plots of the raw data used to extract the critical magnetic field of NbN. (a) is for an out-of-plane magnetic field and (b) is for an in-plane magnetic field.

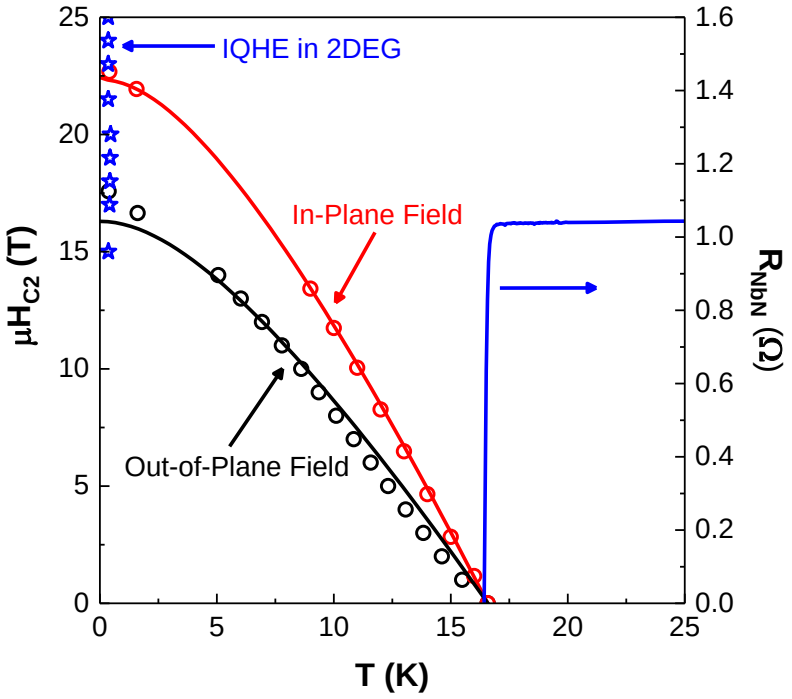

Fig. S7. A plot of H_{c2} vs. T of the buried NbN layer. Black circles are for an out-of-plane magnetic field, and red circles are for an in-plane magnetic field. The black (out-of-plane field) and red (in-plane field) lines are fits (*37-39*) to the Maki-de Gennes formula $\ln\left(\frac{T}{T_c}\right) = \psi\left(\frac{1}{2}\right) - \psi\left(\frac{1}{2} + \frac{\hbar D H_{c2}^{\parallel}(T)}{2\phi_0 k_B T}\right)$, where ψ is the polygamma function, ϕ_0 is the magnetic flux quantum, and D is the electron diffusion constant for electrons in the normal state. We find D is equal to 0.143 m^2/s and 0.104 m^2/s for the out-of-plane and in-plane fields, respectively. From the fit, we extract a superconducting coherence length of ~4.5 nm for out-of-plane magnetic fields and ~3.8 nm for in-plane magnetic fields from $H_{c2}(0) = \frac{\phi_0}{2\pi\xi^2}$. Because the mean free path of ~1 nm (*5*) is smaller than the coherence length, and both are much smaller than the NbN film thickness, we justify this fit *a posteriori*. The blue stars indicate temperatures and magnetic fields where the IQHE was experimentally observed. The blue line shows the resistance of the NbN layer as a function of temperature.

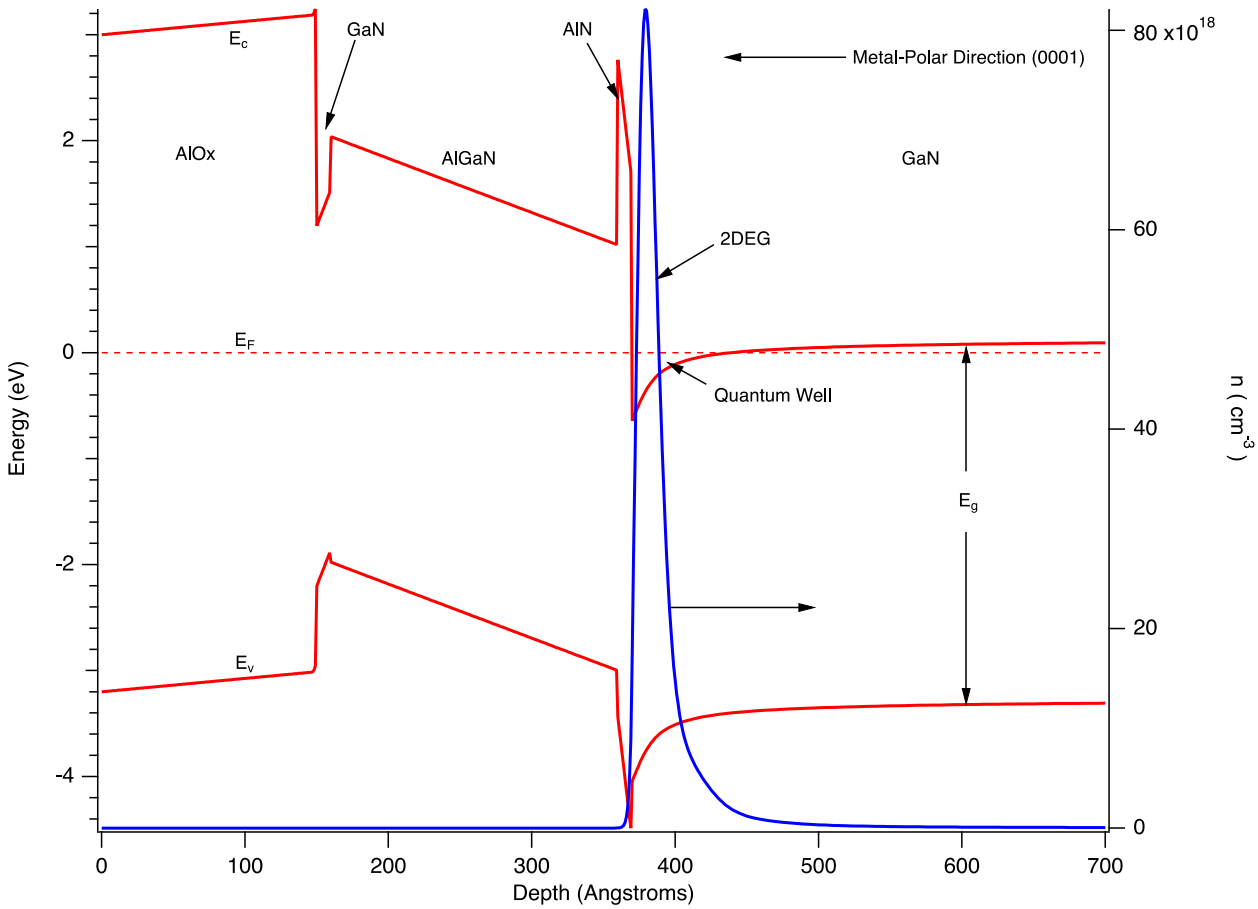

Fig. S8. Energy band diagram of the gated AlGaN/AlN/GaN epitaxial nitride heterostructure in which the 2DEG exhibiting IQHE is formed. The spatially resolved electron density is on the right axis. The spike in the electron density shows where the 2DEG forms in the quantum well.

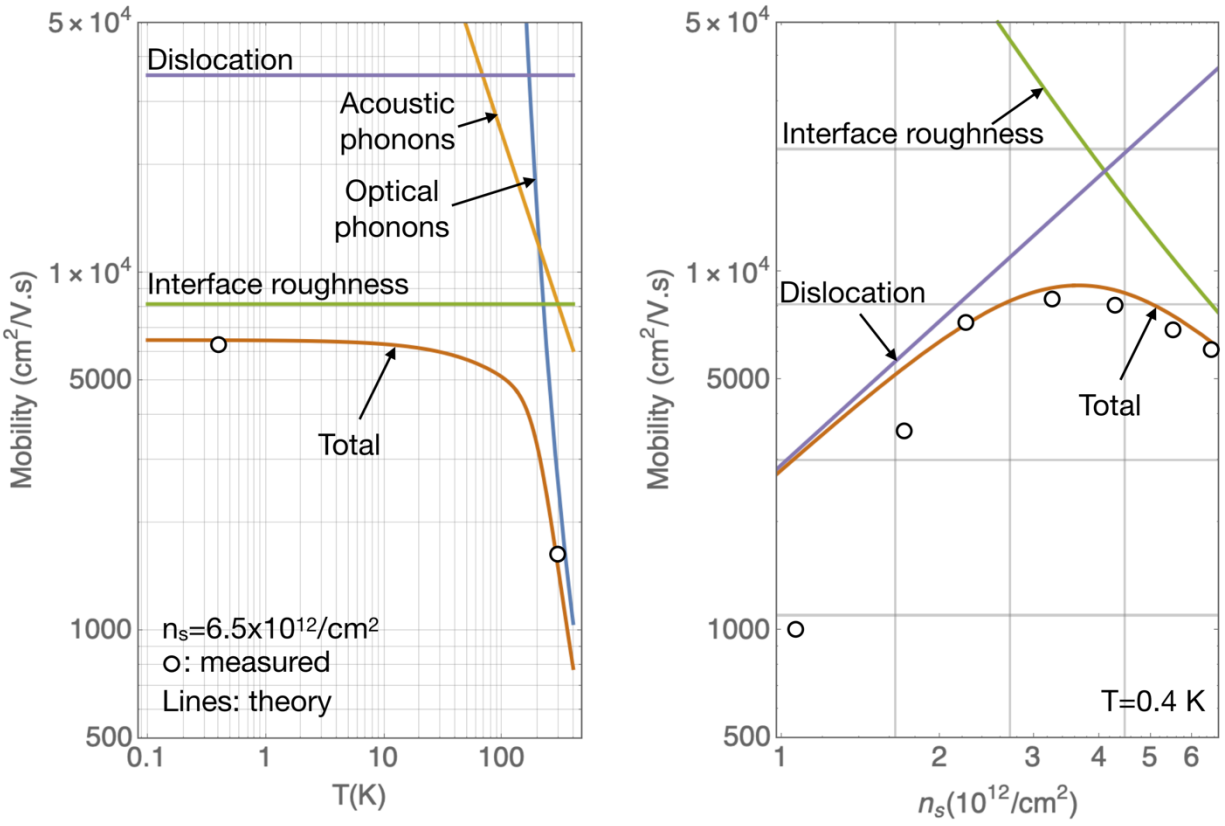

Fig. S9. Measured and calculated electron mobilities of the 2DEG which exhibits IQHE. The colored lines are theoretical calculations for various scattering mechanisms. The black circles are experimental electron mobilities that were extracted from Hall-effect measurements.

REFERENCES AND NOTES

1. K. v. Klitzing, G. Dorda, M. Pepper, New method for high-accuracy determination of the fine-structure constant based on quantized Hall resistance. *Phys. Rev. Lett.* **45**, 494–497 (1980).
2. D. J. Thouless, M. Kohmoto, M. P. Nightingale, M. den Nijs, Quantized Hall conductance in a two-dimensional periodic potential. *Phys. Rev. Lett.* **49**, 405–408 (1982).
3. J. Clarke, F. K. Wilhelm, Superconducting quantum bits. *Nature* **453**, 1031–1042 (2008).
4. B. N. Taylor, New measurements standards for 1990. *Phys. Today* **42**, 23–26 (1989).
5. R. Yan, G. Khalsa, S. Vishwanath, Y. Han, J. Wright, S. Rouvimov, D. Scott Katzer, N. Nepal, B. P. Downey, D. A. Muller, H. G. Xing, D. J. Meyer, D. Jena, GaN/NbN epitaxial semiconductor/superconductor heterostructures. *Nature* **555**, 183–189 (2018).
6. C. Wood, D. Jena, *Polarization Effects in Semiconductors* (Springer US, 2008).
7. W. E. Carlos, J. A. Freitas Jr., M. A. Khan, D. T. Olson, J. N. Kuznia, Electron-spin-resonance studies of donors in wurtzite GaN. *Phys. Rev. B* **48**, 17878–17884 (1993).
8. T. Ando, Y. Uemura, Theory of oscillatory g factor in an MOS inversion layer under strong magnetic fields. *J. Phys. Soc. Jpn.* **37**, 1044–1052 (1974).
9. N. Tang, K. Han, F.-C. Lu, J.-X. Duan, F.-J. Xu, B. Shen, Exchange enhancement of spin-splitting in $Al_xGa_{1-x}N$/GaN heterostructures in tilted magnetic fields. *Chin. Phys. Lett.* **28**, 037103 (2011).
10. D. Jena, I. Smorchkova, A. C. Gossard, U. K. Mishra, Electron transport in III-V nitride two-dimensional electron gases. *Phys. Status Solidi B* **228**, 617–619 (2001).
11. D. Jena, U. K. Mishra, Quantum and classical scattering times due to charged dislocations in an impure electron gas. *Phys. Rev. B* **66**, 241307(R) (2002).
12. M. J. Manfra, L. N. Pfeiffer, K. W. West, H. L. Stormer, K. W. Baldwin, J. W. P. Hsu, D. V. Lang, R. J. Molnar, High-mobility AlGaN/GaN heterostructures grown by molecular-beam epitaxy on GaN templates prepared by hydride vapor phase epitaxy. *Appl. Phys. Lett.* **77**, 2888–2890 (2000).
13. M. J. Manfra, K. W. Baldwin, A. M. Sergent, R. J. Molnar, J. Caissie, Electron mobility in very low density GaN/AlGaN/GaN heterostructures. *Appl. Phys. Lett.* **85**, 1722–1724 (2004).
14. M. J. Manfra, K. W. Baldwin, A. M. Sergent, K. W. West, R. J. Molnar, J. Caissie, Electron mobility exceeding 160000 cm^2/Vs in AlGaN/GaN heterostructures grown by molecular-beam epitaxy. *Appl. Phys. Lett.* **85**, 5394–5396 (2004).
15. C. Skierbiszewski, K. Dybko, W. Knap, M. Siekacz, W. Krupczynski, G. Nowak, M. Bockowski, J. Lusakowski, Z. R. Wasilewski, D. Maude, T. Suski, S. Porowski, High mobility two-dimensional

electron gas in AlGaN/GaN heterostructures grown on bulk GaN by plasma assisted molecular beam epitaxy. *Appl. Phys. Lett.* **86**, 102106 (2005).

16. S. Schmult, M. J. Manfra, A. M. Sergent, A. Punnoose, H. T. Chou, D. Goldhaber-Gordon, R. J. Molnar, Quantum transport in high mobility AlGaN/GaN 2DEGs and nanostructures. *Phys. Status Solidi B* **243**, 1706–1712 (2006).
17. D. Jena, K. Banerjee, G. H. Xing, 2D crystal semiconductors: Intimate contacts. *Nat. Mater.* **13**, 1076–1078 (2014).
18. J. Guo, Y. Cao, C. Lian, T. Zimmermann, G. Li, J. Verma, X. Gao, S. Guo, P. Saunier, M. Wistey, D. Jena, H. Xing, Metal-face InAlN/AlN/GaN high electron mobility transistors with regrown ohmic contacts by molecular beam epitaxy. *Phys. Status Solidi A* **208**, 1617–1619 (2011).
19. J. Guo, G. Li, F. Faria, Y. Cao, R. Wang, J. Verma, X. Gao, S. Guo, E. Beam, A. Ketterson, M. Schuette, P. Saunier, M. Wistey, D. Jena, H. Xing, MBE-regrown ohmics in InAlN HEMTs with a regrowth interface resistance of 0.05Ω-mm. *IEEE Electron Device Lett.* **33**, 525–527 (2012).
20. F. Afroz Faria, J. Guo, P. Zhao, G. Li, P. Kumar Kandaswamy, M. Wistey, H. Xing, D. Jena, Ultra-low resistance ohmic contacts to GaN with high Si doping concentrations grown by molecular beam epitaxy. *Appl. Phys. Lett.* **101**, 032109 (2012).
21. E. Kamińska, A. Piotrowska, M. Guziewicz, S. Kasjaniuk, A. Barcz, E. Dynowska, M. D. Bremser, O. H. Nam, R. F. Davis, Ohmic contact to n-GaN with TiN diffusion barrier. *MRS Proc.* **449**, 1055 (1996).
22. G. Vanko, T. Lalinský, Ž. Mozolová, J. Liday, P. Vogrinčič, A. Vincze, F. Uherek, Š. Haščík, I. Kostič, Nb-Ti/Al/Ni/Au based ohmic contacts to AlGaN/GaN. *Vacuum* **82**, 193–196 (2007).
23. P. Rickhaus, M. Weiss, L. Marot, C. Schönenberger, Quantum Hall effect in graphene with superconducting electrodes. *Nano Lett.* **12**, 1942–1945 (2012).
24. K. Komatsu, C. Li, S. Autier-Laurent, H. Bouchiat, S. Guéron, Superconducting proximity effect in long superconductor/graphene/superconductor junctions: From specular Andreev reflection at zero field to the quantum Hall regime. *Phys. Rev. B* **86**, 115412 (2012).
25. Z. Wan, A. Kazakov, M. J. Manfra, L. N. Pfeiffer, K. W. West, L. P. Rokhinson, Induced superconductivity in high-mobility two-dimensional electron gas in gallium arsenide heterostructures. *Nat. Commun.* **6**, 7426 (2015).

26. G.-H. Lee, K.-F. Huang, D. K. Efetov, D. S. Wei, S. Hart, T. Taniguchi, K. Watanabe, A. Yacoby, P. Kim, Inducing superconducting correlation in quantum Hall edge states. *Nat. Phys.* **13**, 693–698 (2017).
27. J. Zhi, N. Kang, F. Su, D. Fan, S. Li, D. Pan, S. P. Zhao, J. Zhao, H. Q. Xu, Coexistence of induced superconductivity and quantum Hall states in InSb nanosheets. *Phys. Rev. B* **99**, 245302 (2019).
28. V. E. Calado, S. Goswami, G. Nanda, M. Diez, A. R. Akhmerov, K. Watanabe, T. Taniguchi, T. M. Klapwijk, L. M. K. Vandersypen, Ballistic Josephson junctions in edge-contacted graphene. *Nat. Nanotechnol.* **10**, 761–764 (2015).
29. F. Amet, C. T. Ke, I. V. Borzenets, J. Wang, K. Watanabe, T. Taniguchi, R. S. Deacon, M. Yamamoto, Y. Bomze, S. Tarucha, G. Finkelstein, Supercurrent in the quantum Hall regime. *Science* **352**, 966–969 (2016).
30. P. Krogstrup, N. L. B. Ziino, W. Chang, S. M. Albrecht, M. H. Madsen, E. Johnson, J. Nygård, C. M. Marcus, T. S. Jespersen, Epitaxy of semiconductor-superconductor nanowires. *Nat. Mater.* **14**, 400–406 (2015).
31. S. D. Sarma, M. Freedman, C. Nayak, Majorana zero modes and topological quantum computations. *npq Quant. Inf.* **1**, 15001 (2015).
32. J. Shabani, M. Kjaergaard, H. J. Suominen, Y. Kim, F. Nichele, K. Pakrouski, T. Stankevic, R. M. Lutchyn, P. Krogstrup, R. Feidenhans'l, S. Kraemer, C. Nayak, M. Troyer, C. M. Marcus, C. J. Palmstrøm, Two-dimensional epitaxial superconductor-semiconductor heterostructures: A platform for topological superconducting networks. *Phys. Rev. B* **93**, 155402 (2016).
33. M. Kjaergaard, F. Nichele, H. J. Suominen, M. P. Nowak, M. Wimmer, A. R. Akhmerov, J. A. Folk, K. Flensberg, J. Shabani, C. J. Palmstrøm, C. M. Marcus, Quantized conductance doubling and hard gap in a two-dimensional semiconductor-superconductor heterostructure. *Nat. Commun.* **7**, 12841 (2016).
34. S. M. Frolov, M. J. Manfra, J. D. Sau, Topological superconductivity in hybrid devices. *Nat. Phys.* **16**, 718–724 (2020).
35. M. S. Miao, Q. Yan, C. G. Van de Walle, W. K. Lou, L. L. Li, K. Chang, Polarization-driven topological insulator transition in a GaN/InN/GaN quantum well. *Phys. Rev. Lett.* **109**, 186803 (2012).
36. G. A. Antcliffe, R. A. Straddling, De Haas-Shubnikov effect in In Sb with high electron concentrations. *Phys. Lett.* **20**, 119–121 (1966).

37. P. G. de Gennes, Behavior of dirty superconductors in high magnetic fields. *Phys. Kondens. Mater.* **3**, 79–90 (1964).
38. K. Maki, The magnetic properties of superconducting alloys I. *Physics* **1**, 21–30 (1964).
39. A. Godeke, M. C. Jewell, A. A. Golubov, B. Ten Haken, D. C. Larbalestier, Inconsistencies between extrapolated and actual critical fields in Nb_3Sn wires as demonstrated by direct measurements of H_{c2}, H^* and T_c. *Supercond. Sci. Technol.* **16**, 1019–1025 (2003).